Journal of Alloys and Compounds 506 (2010) 831–840

Contents lists available at ScienceDirect

Journal of Alloys and Compounds

journal homepage: www.elsevier.com/locate/jallcom

Comparisons of metallic clusters imbedded in the surface oxide of AB_2, AB_5, and A_2B_7 alloys

K. Young [a,*], B. Huang [a], R.K. Regmi [b], G. Lawes [b], Y. Liu [c]

[a] Energy Conversion Devices Inc./Ovonic Battery Company, 2983 Waterview Drive, Rochester Hills, MI 48309, USA
[b] Department of Physics and Astronomy, Wayne State University, Detroit, MI 48201, USA
[c] Department of Chemistry, Wayne State University, 5101 Cass Ave., Detroit, MI 48202, USA

ARTICLE INFO

Article history:
Received 29 March 2010
Received in revised form 8 July 2010
Accepted 9 July 2010
Available online 16 July 2010

Keywords:
Hydrogen absorbing materials
Transition metal alloys
Metal hydride electrode
Electrochemical reactions

ABSTRACT

In order to clarify the relationship between the saturation magnetization of the activated metal hydride material and electrode performance, the specific power measured at both low temperature (−30 °C) and operating temperature (35 °C) of a nickel metal hydride battery were compared with magnetization measurements. It is found specific powers measured at both temperatures correlate well with the saturated magnetic susceptibility, which is proportional to the total amount of metallic nickel clusters distributed within the surface oxide layer after activation. Both the gas phase storage and electrochemical properties of the activated AB_2, AB_5, and A_2B_7 alloys were investigated. While the AB_2 alloy has the highest storage capacity, it also has the lowest high-rate dischargeability among the three alloys. This suggests a competition between storage capacity and rate capability in these materials. In an alkaline etching experiment, it is established the saturation magnetization increases with etching time in these AB_2, AB_5, and A_2B_7 alloys. The saturation magnetization after a 4 h etches track the changes in the high-rate dischargeability. The increase is attributed to the growth in size of the metallic inclusions for the AB_2 and Nd–A_2B_7 samples, and from an increase in the number of metallic inclusion in the case of AB_5 and La–A_2B_7. Transmission electron microscope studies calibrate the size inferred from magnetic susceptibility studies and also the Ni-dominated FCC structure of the metallic clusters.

1. Introduction

The Misch-metal based AB_5 hydrogen storage alloy is the conventional choice for metal hydride (MH) electrode material used in nickel metal hydride (Ni/MH) batteries [1–7]. However, the limited discharge capacity of this alloy has prompted a search for alternative materials with higher hydrogen storage capacities. Of these systems, the AB_2 and A_2B_7 alloys are considered the most promising candidates [8–20]. A careful comparison of the structural and physical characteristics of these various alloys is necessary to identify the fundamental differences and to suggest methods for further improving their properties. This paper presents results from the comparison of the AB_2, AB_5, and A_2B_7 alloys in gas phase and electrochemical testing; and also presents analytical results of the surface metallic clusters.

The metallic nickel clusters embedded in the surface oxide layer of the AB_2 [21–26] and AB_5 [27–38] MH electrodes as the product of a self restoration [27,30] are known to play a very important role in catalyzing the electrochemical reaction powering Ni/MH batteries. These Ni-based clusters not only control the high-rate dischargeability (HRD) of the electrodes but also increase the corrosion/passivation resistance of the alloy [13,39]. Extensive measurements of magnetization together with transmission electron microscopy (TEM) studies were used to investigate the properties of these superparamagnetic Ni-based clusters [25,28,30,31,34,38,40]. Based on fits of the sample magnetization to the Langevin function, the sizes of these Ni clusters were estimated to range from a 2 to 20 nm, depending on the alkaline treatment conditions [38]. The total volume percentage of these Ni rich clusters, reaching up to 5 wt.% [41], can be extracted from the value of the saturation magnetization, M_S, normalized to the magnetization for pure nickel metal. This assumes the magnetic signal is entirely due to the Ni clusters, which is reasonable as the magnetization of the pure alloy is seven orders of magnitude smaller than that of metallic nickel [28]. The magnetic characteristics of the alloy have been used extensively to parameterize surface catalytic activity in this class of materials [39,41–47]. The elemental composition of these Ni-based metallic clusters, as determined by TEM studies, varies from pure Ni [32,48,49], to Ni–Co [36], Ni–Co–Fe [37], Ni–Mn [50], and more complicated Ni–Co–Cu highly disordered alloys [24]. The metallic nature of these clusters was confirmed by electron energy loss spectroscopy [23], X-ray diffraction (XRD) [16], X-ray

* Corresponding author. Tel.: +1 248 293 7000; fax: +1 248 299 4520.
E-mail address: kwoyoung@yahoo.com (K. Young).

0925-8388/$ – see front matter © 2010 Elsevier B.V. All rights reserved.
doi:10.1016/j.jallcom.2010.07.086

photoemission spectroscopy (XPS) [51–53], and high-resolution TEM with select area electron diffraction [54]. XPS was also used to study the electrochemical activity of the surface [55]. These Ni-based clusters can be formed during the activation/formation cycle of the battery [43,56,57], an oxidizing agent [58], alkaline conditions [59], and other surface treatments [60–69]. While the superparamagnetic response can provide insight into the nanoscale structure of the metallic clusters in these electrodes, the paramagnetic component of the magnetic susceptibility has been used previously to quantify the electron concentration of the partially hydride $LaNi_5$ alloy [70]. In this paper, the properties extracted from the magnetic measurements will be compared and correlated to the gas phase and electrochemical properties among AB_2, AB_5, and A_2B_7 alloys.

2. Experimental setup

Ingot samples were prepared by conventional induction melting (25 kg) with a steel pancake-shape mold in an argon atmosphere. The chemical composition of each sample was determined using a Varian *Liberty* 100 inductively coupled plasma (ICP) system.

Pressure–Concentration–Temperature (PCT) characteristics for each sample was measured using a Suzuki-Shokan multi-channel PCT system. In the PCT analysis, each sample was first activated by a 2-h thermal cycle between 300 °C and room temperature at 25 atm H_2 pressure. Magnetic susceptibility measurements were performed using a Quantum Design MPMS-5T SQUID magnetometer, a Quantum Design PPMS 9 T with the acms option, and a Princeton Measurements Corporation MicroMag 2900 alternating gradient magnetometer from a sample having a mass of 25–35 mg. Details of the half-cell and C-size Ni/MH full cell construction and measurement have been described previously [14,71]. Specific power for these sealed Ni/MH batteries was measured using a pulse-discharge method with a 10 s 10C discharge at 80% of state-of-charge.

A TEM system (Jeol-2010 FasTEM, JEOL Inc.) with X-ray energy dispersive spectroscopy (EDS) (EDAX Inc.) capability was used to study the size, crystal structure, and composition of the metallic inclusions embedded in the surface oxide. The powder samples were first loaded in a copper tube with M-Bond 610 epoxy, with the diameter of the copper being 3 mm. After several hours' curing, the copper tube filled with hardened powders was sliced using a low speed diamond saw, which provides a minimal disruption of the sample microstructure. The slices were then reduced in thickness by mechanical grinding and polishing and were finally thinned by ion-beam milling at 5 kV (Gatan PIPs 691 ion-beam milling machine). The TEM studies were conducted with a beam energy of 200 keV.

3. Results and discussion

3.1. Saturation magnetization and specific power

Ten Misch-metal based AB_5 alloys were prepared according to the target formulas listed in Table 1. The original intent for this batch of alloys was to improve the low temperature specific power of the AB_5 alloy by introducing Cu, Zr, and/or Si additives [72,73]. These alloys were annealed in vacuum (1×10^{-8} Torr) at 960 °C for 8 h before mechanical crushing into −200 mesh powder. The powder was etched at 100 °C in 60% KOH for 1 h to activate the alloy surface. The room temperature magnetic susceptibility was measured using the MicroMag 2900 magnetometer. The M_S value was estimated from the $M(H)$ curves after subtracting the high field linear component, which corresponds to the paramagnetic contribution. These values are listed in Table 1. From these studies, it is found that the M_S values of the substituted alloys are higher than those measured for the parent alloy without any Cu, Zr, or Si. The specific powers of Ni/MH batteries made from these alloys at two temperatures, −30 °C and 35 °C, are listed in Table 1 and plotted against the M_S values in Fig. 1. From this figure, we can see that peak power measured at both temperatures increase with the increase in the M_S values. In the case of low temperature peak power, the amount of surface nickel inclusion is not the only significant factor. Both the shape and proximity of the voids in the surface oxide also play very important role from an earlier study [24].

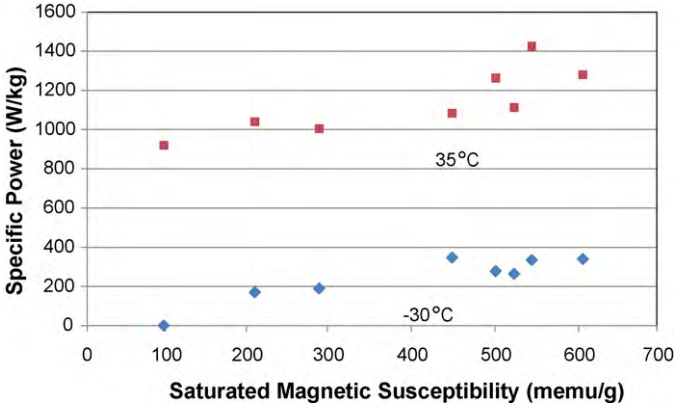

Fig. 1. Specific power measured at 35 °C and −30 °C of a series of AB_5 alloys as functions of the saturated magnetic susceptibility measured at room temperature.

3.2. Comparison of the gas phase storage properties

Four distinct alloys were made by induction melting. Alloy A, with a nominal composition of $Ti_{12}Zr_{21.5}Ni_{36.2}V_{9.5}Cr_{4.5}Mn_{13.6}Sn_{0.3}Co_2Al_{0.4}$, is a typical C14-dominated AB_2 alloy with the electrochemical properties reported in full elsewhere [71]. This alloy has a good combination of storage capacity and rate capability. Alloy B, with a nominal composition of $La_{10.5}Ce_{4.3}Pr_{0.5}Nd_{1.4}Ni_{60.0}Co_{12.7}Mn_{5.9}Al_{4.7}$, is a La-rich Misch-metal based AB_5 alloy widely used in current high power applications for commercial Ni/MH batteries [74]. Alloy C, with a nominal composition of $La_{16.3}Mg_{7.0}Ni_{65.1}Co_{11.6}$ is the first high capacity A_2B_7 alloy reported in that family [75]. This alloy only contains one rare earth element, La, instead of the combination of four in Alloy B. Alloy D, another A_2B_7 alloy with a nominal composition of $Nd_{18.8}Mg_{2.5}Ni_{65.0}Al_{3.6}$, also contains only one rare earth element, Nd. Both Co and Mn are excluded to minimize the self-discharge of the battery [76]. The amount of Mg is adjusted to produce a suitable hydrogen–metal bond strength for Ni/MH applications. Alloy A was prepared without annealing, while Alloy B was annealed in vacuum (1×10^{-8} Torr) at 960 °C for 8 h. Both alloys C and D were annealed in 1 atm of argon at 900 °C for 5 h to prevent the excessive loss of Mg through vaporization.

Table 1
Ten AB_5 alloys with the measured saturated magnetic susceptibility after 1 h etch in 100 °C 60% KOH solution and specific powers measured at −30 and 35 °C.

Formula (in atomic percentage)	Saturated magnetic susceptibility (memu/g)	Specific power measured at −30 °C (W/kg)	Specific Power Measured at 35 °C (W/kg)
$La_{10.5}Ce_{4.3}Pr_{0.5}Nd_{1.4}Ni_{60.0}Co_{12.7}Mn_{5.7}Al_{4.7}$	98	0	920
$La_{10.5}Ce_{4.3}Pr_{0.5}Nd_{1.4}Ni_{64.3}Co_{3.0}Mn_{4.6}Al_{6.0}Cu_{5.4}$	210	170	1040
$La_{10.5}Ce_{4.3}Pr_{0.5}Nd_{1.4}Ni_{64.3}Co_{5.0}Mn_{4.6}Al_{6.0}Cu_{3.4}$	290	190	1005
$La_{10.5}Ce_{4.3}Pr_{0.5}Nd_{1.4}Ni_{64.2}Co_{4.9}Mn_{4.5}Al_{5.9}Cu_{3.3}Si_{0.5}$	449	347	1084
$La_{10.5}Ce_{4.3}Pr_{0.5}Nd_{1.4}Ni_{64.3}Co_{5.0}Mn_{4.6}Al_{6.0}Cu_{3.2}Zr_{0.2}$	501	278	1263
$La_{9.6}Ce_{3.9}Pr_{0.5}Nd_{1.3}Ni_{65.8}Co_{4.6}Mn_{4.2}Al_{5.5}Cu_{4.6}$	523	264	1113
$La_{10.5}Ce_{4.0}Pr_{0.5}Nd_{1.4}Ni_{64.3}Co_{5.0}Mn_{4.6}Al_{6.0}Cu_{2.9}Zr_{0.5}$	544	335	1425
$La_{10.5}Ce_{4.3}Pr_{0.5}Nd_{1.4}Ni_{64.1}Co_{8.2}Mn_{4.3}Al_{5.7}Si_{1.0}$	605	340	1280

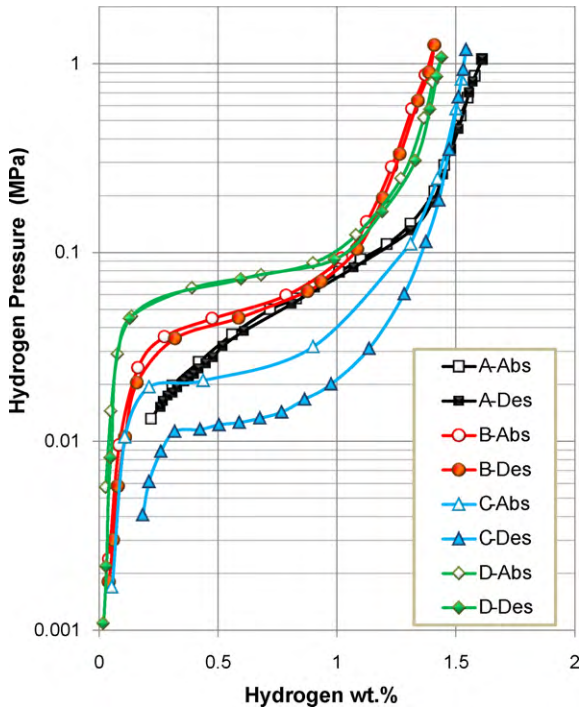

Fig. 2. PCT 30 °C absorption (open symbols) and desorption (filled symbols) isotherms for alloys A–D.

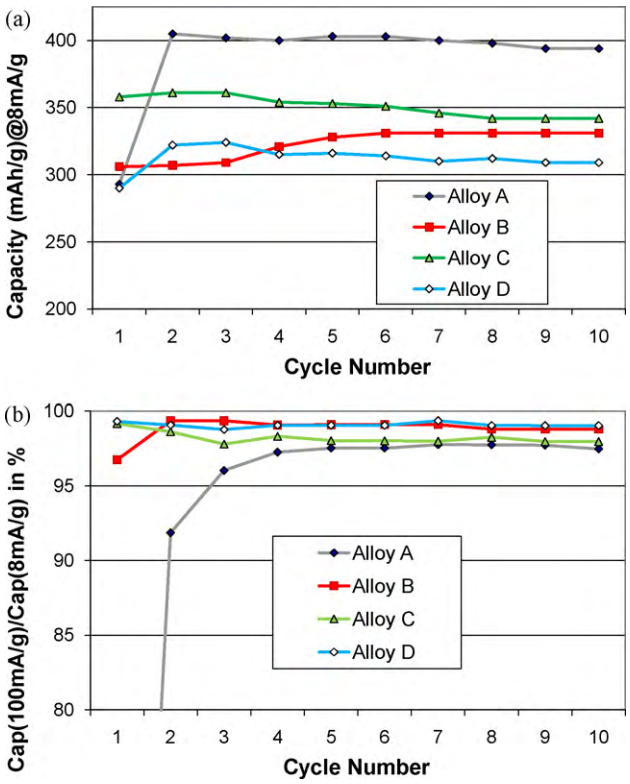

Fig. 3. Evolution of (a) full discharge capacity at a rate of 8 mA/g, (b) HRD defined the ratio of capacity obtained at 100 mA/g vs. capacity obtained at 8 mA/g as functions of cycle number for alloys A–D.

The 30 °C PCT isotherms of the four alloys are shown in Fig. 2. The isotherms for Alloy A have both the highest total storage capacity and largest plateau slope. Alloy C has the second highest total storage capacity followed by Alloy D. The lowest total storage capacity is found in Alloy B, emphasizing the need to search for alternative alloys with higher capacity. The large value of the plateau slope in Alloy A indicates a higher degree of disorder, consistent with this sample being the only one prepared without thermal annealing [14]. This degree of disorder is compatible with Alloy A exhibiting the typical multi component nature found in many AB_2 alloys [21]. Both Alloys C and D, which have only one rare earth element in their composition, exhibit much smaller plateau slopes. Alloy B, with four rare earth elements, only allows the dominant $CaCu_5$ crystal structure, therefore exhibiting a smaller plateau slope consistent with less disorder.

The equilibrium plateau pressure is related to the average hydrogen–metal bond strength, ease of hydride dissociation, and open-circuit voltage as in an electrochemical cell. The plateau pressures of all these alloys can be fine-tuned by adjusting the Ti/Zr, La/Ce, La/Mg, and Nd/Mg contents. For this set of alloys, the plateau pressures in decreasing order are found in Alloy D, then B, then A, with Alloy C having the lowest pressure. This means that hydrogen is released most readily from Alloy D during discharge. A higher plateau pressure also suggests a higher open-circuit voltage. The hysteresis of Alloy A is slightly smaller than that of Alloy B. Both of these are larger than the hysteresis found in Alloy D but smaller than that for Alloy C. Based on these values for the hysteresis, the alloys having the greatest mechanical stability against pulverization during cycling are: Nd–A_2B_7, AB_5, AB_2, La–A_2B_7 in decreasing order, as determined in previous studies [15,77]. One particularly interesting fact worth mentioning is that although Alloy D has the smallest hydrogen storage capability, it exhibits an exceptionally rapid increase in the equilibrium pressure in the α-region (corresponding to the protons dispersing randomly in the alloy) of the PCT curve. This specific response makes Alloy D an excellent candidate material for low self-discharge designs due to the capability of maintaining a relatively high potential at the end of a discharge cycle.

3.3. Comparison of the electrochemical properties

3.3.1. Half-cell

A small electrode, having an area of about 1 cm^2, was used to study the activation, capacity, and high-rate dischargeability (HRD) of these four alloys. Capacities from the slowest rate discharge current (8 mA/g) for the first 10 cycles for each alloy are plotted in Fig. 3a. Alloys A and D require one activation cycle to reach the capacity plateau while Alloys B and C immediately achieve the capacity plateau with the very first cycle. On further cycling, Alloy B enters a second plateau having a higher capacity. The maximum discharge capacity at 8 mA/g is summarized in Table 2. As expected, the evolution of discharge capacity essentially follows the same trend as the maximum hydrogen storage, as measured by analyzing the PCT curves. The alloy capacities are ordered as: A (AB_2), C (La–A_2B_7), B (AB_5), D (Nd–A_2B_7) in decreasing order. These measurements reflect the high capacities typically observed in AB_2 alloys.

The half-cell HRD was determined by taking the ratio between the discharge capacities at 100 mA/g and at 8 mA/g. These results for the first 10 cycles are plotted in Fig. 3b. The number of cycles required for the Alloys A–D to reach the HRD plateaus are 5, 2, 1, and 1, respectively. These results support the suggestion that higher Ni content in the alloy facilitates the initial power formation, when the number of cycles to reach the HRD is compared with the Ni content of the alloys (A-38 at%, B-60 at%, C and D-65 at%). X-ray photoemission spectroscopy studies find that the abundance of Ni at the surface was reported to be an important parameter in determining the activation of alloys [78]. For comparison, the HRD values obtained at the third cycle are listed

Table 2
Compositions and summary of properties of Alloys A–D. Last three qualities were measured after 4 h etch in 30% KOH at 100 °C.

Alloys	Composition	Alloy system	Maximum hydrogen storage wt. %	Plateau pressure (MPa)	Discharge Cap @ 8 mA/g (mA h/g)	Cap (100 mA/g)/ Cap (8 mA/g) (%) @ 3rd cycle	Exchange current (mA/g)	Diffusion coefficient ($\times 10^{-11}$ cm^2/s)	Total Solute Conc. (ppm)	Saturated magnetic susceptibility (memu/g)	Normalized cluster size
A	$Ti_{12}Zr_{21.5}Ni_{36.2}V_{9.5}Cr_{4.5}Mn_{13.6}Sn_{0.3}Co_2Al_{0.4}$	AB_2	1.61	0.045	403	96.0%	32.1	9.7	112.3	33	1.00
B	$La_{10.5}Ce_{4.3}Pr_{0.5}Nd_{1.4}Ni_{60.0}Co_{12.7}Mn_{5.9}Al_{4.7}$	AB_5	1.41	0.055	331	99.3%	43.2	25.5	118.3	434	0.93
C	$La_{16.3}Mg_{7.0}Ni_{65.1}Co_{11.6}$	A_2B_7	1.54	0.018	361	97.8%	41.0	30.8	19.4	369	1.06
D	$Nd_{18.8}Mg_{2.5}Ni_{65.1}Al_{3.6}$	A_2B_7	1.44	0.081	324	98.8%	22.7	11.4	101.7	132	0.95

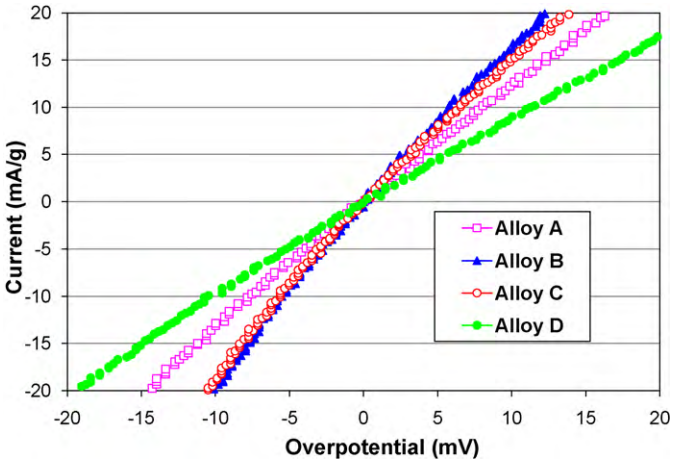

Fig. 4. Linear polarization curves for alloys A–D.

in Table 2 for each alloy and will be discussed in the sections below.

3.3.2. Surface reaction

One way to probe the HRD is to measure the surface reaction and the bulk transport properties of the alloys. The exchange current (I_0), which is a measure of the kinetics for the electrochemical hydrogen reaction at the surface of the electrode, was calculated from the electrode polarization using a method described previously [40]. Electrode samples were cycled 10 times to ensure full activation. The linear polarization curves at 50% depth-of-discharge are shown in Fig. 4 and the calculated exchange currents are listed in Table 2. They are in the following order: B (43.2 mA/g) > C (41.0 mA/g) > A (32.1 mA/g) > D (22.7 mA/g). The higher exchange current in AB_5 alloys than in AB_2 alloys has been reported previously [79], with a comparison of Cole–Cole plots also indicating higher reaction resistance for AB_2 alloys as opposed to AB_5 alloys [80]. The Mn and Co in the AB_5 alloy help promote the surface reaction. La is the most chemically reactive element in rare earth family and is known to produce a highly reactive surface suitable for high-rate application [81–83]. Because of this effect, Alloy C, which has a high La-content, has the second highest surface exchange current. Ni content also has a strong effect on the surface reaction [84–86]. With the lowest Ni content of these compounds, Alloy A shows the third largest surface exchange current. Alloy D, having no Mn or Co, was originally designed to minimize the leaching of soluble ions into electrolyte [76], and shows the least surface reaction of these compounds.

3.3.3. Bulk hydrogen diffusion

Bulk transport properties can be studied by measuring the hydrogen diffusion coefficient using a potentiostatic discharge method described previously [14]. The diffusion coefficient was calculated from the semi-logarithmic behavior of the current response vs. time at larger times, where the transport is dominated by diffusion ($t > 2000$ s). These values are listed in Table 2, where the alloys with diffusion constants in decreasing order, are: C (30.8×10^{-11} cm^2/s) > B (25.5×10^{-11} cm^2/s) > D (11.4×10^{-11} cm^2/s) > A (9.7×10^{-11} cm^2/s). The transport of hydrogen governed by quantum-mechanical tunneling [87] depends not only by the size of the hydrogen occupation sites and the distance between the neighboring sites [88,89] but also the degree of disorder in the material since the grain boundary can either facilitate or hinder the hydrogen motion [90,91]. The general result of a higher diffusion coefficient for hydrogen in multi-element AB_5 (6.2×10^{-9} cm^2/s, $LaNi_4Cr_{0.4}Mn_{0.3}Al_{0.3}$) as

compared to AB_2 (1.1×10^{-9} cm^2/s, $ZrNi_{1.2}Mn_{0.4}Cr_{0.4}$) has been reported previously in a micro-electrochemical study [92].

3.3.4. High-rate dischargeability

As indicated in Table 2, the HRD values vary from alloy to alloy, with the rate being highest for alloys B(AB_5) followed by D(A_2B_7), C(A_2B_7), and A(AB_2) in order. This trend does not appear to directly correlate with any single property related to the gas phase storage or electrochemical response, as seen from the rankings listed in Table 4. The magnitude of the half-cell HRD varies systematically with the product of the plateau pressure (PP) and exchange current (EC). The output power is measured in watts, which is the product of voltage and current. While the current is measured directly, the voltage must be extracted from log of plateau pressure using the Nernst equation:

$$E\,\mathrm{eq}(M/MH) - E\,\mathrm{eq}(H_2O/Hg) = -0.9324 - 0.0329 \log P_{H2}$$

With this analysis, the relationship between half-cell HRD and the product of PP and EC is to be expected. The correlation between the HRD and metallic surface clusters will be investigated in detail in the next section.

3.4. Metallic Ni clusters embedded in surface oxide

3.4.1. Hot alkaline etching

Conditioning samples in a hot alkaline bath is a technique that has been used extensively in activating the hydrogen storage alloy surface [50,59,81,93]. Details about an etching experiment carried in a 30% KOH bath at 100 °C are presented in depth elsewhere [14]. The concentration of various metal components in the resultant solutes was measured by ICP analysis and the results are listed in Table 3. The results are consistent with report given by Wu et al. on a $Ti_{0.35}Zr_{0.65}Ni_{1.2}V_{0.6}Mn_{0.2}Cr_{0.2}$ alloy [81]. The majority of the elements leached out from Alloy A are Zr, V, and Al with their concentration in the batch increasing with the etching time. It is believed Zr and V are the first constituents to be removed from the AB_2 alloy through this corrosion process. In addition, small concentrations of Ti and Mn were also found in the solution. The concentrations of various metallic components from Alloy A are plotted in Fig. 5 as a function of etching time. The slope of the curve (corrosion rate) is large for the first half-hour then generally decreases as the etching process continues. The chemical reaction generates hydrogen gas at the surface, which is absorbed into the metal and to form a hydride phase inside. This increases the magnitude of the voltage on the negative electrode, slowing down further

Table 3
ICP analysis results for alloys A–D after etching in 100 °C and 30% KOH for various durations. All numbers are concentration in ppm.

Etching time (h)	0.5	1	2	3	4
Alloy A					
Zr	10.2	15.6	32.5	41.6	48.9
V	9.3	11.4	21.4	29.2	33.8
Al	4.5	7.8	13.6	19.2	28.1
Ti	0.3	0.6	0.8	0.9	1
Mn	0.4	0.4	0.4	0.4	0.5
Alloy B					
Al	38	32.4	64.5	88.8	118.3
Mn	0.3	0	0	0.8	0
Ni	0	1.1	0	4.4	0
La	0	0.5	0.1	1.9	0
Alloy C					
La	0	0	0.3	0	6.7
Ni	0	0	0	0	10
Co	0	0	0	0	2.7
Alloy D					
Al	28.4	40.1	51.2	67.8	101
Nd	0	0	0	0	0.7

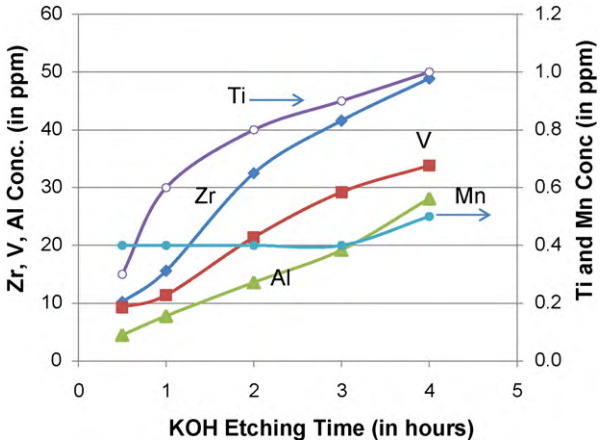

Fig. 5. The solute concentrations of Alloy A as functions of etching time.

Table 4
Ranking of a few parameters related to the power performance of alloys.

Alloy	A	B	C	D
Half-cell HRD	4	1	3	2
Plateau pressure (PP)	3	2	4	1
Exchange current (EC)	3	1	2	4
Diffusion coefficient (DC)	2	4	1	3
PP × EC	9	2	8	4
EC × DC	6	4	2	12
PP × DC	6	8	4	3

oxidation at the surface [94]. The reduction in the corrosion rate is not associated with the metals reaching their saturation limit concentration in the solute, as established by previous calculations [14].

The only major component leached from alloys B and D on hot alkaline etching is Al. The concentration of Al in the solvent also increases monotonically with etching time. However, it should be recalled that Al acts in extending cycle life not by slowing down the corrosion reaction but expanding the lattice and consequently reducing the stress during hydride–dehdride process and creating less pulverization [95]. The concentrations of all other components in the solution are either below or near the detection limit of the ICP instrument.

Alloy C shows the best corrosion resistance in the alkaline etching experiment. Most of the oxidation products are stable as surface oxides/hydroxides. This alloy only shows some measurable corrosion after 4 h of etching, which is believe to coincide with the start of particle pulverization. It is likely the hydrogen formed by oxidizing the surface enters the alloy bulk and cracks the particle to create new surfaces, which are more vulnerable to dissolution. Nickel was reported to be easily oxidized into $Ni(OH)_2$ or $HNiO_2^-$ at the end of discharge at higher temperature [96]. Therefore, in the very beginning of the etching experiment, or when new surface is created as microcracks are formed in the sample, some nickel may be oxidized without the protection in potential from the absorbed hydrogen.

3.4.2. Magnetic measurements

The characteristics of the nanoscale metallic nickel clusters embedded in the surface oxide were studied by probing the magnetic susceptibility. These measurements provide an indirect method of characterizing the size and distribution of the Ni nanoparticles. The magnetization values associated with the ferromagnetic metallic nickel nanoclusters is a few orders of magnitude larger than that from the paramagnetic nickel atoms in the alloy [28]. Room temperature magnetization curves were measured as a function of applied magnetic field for the etched powder samples

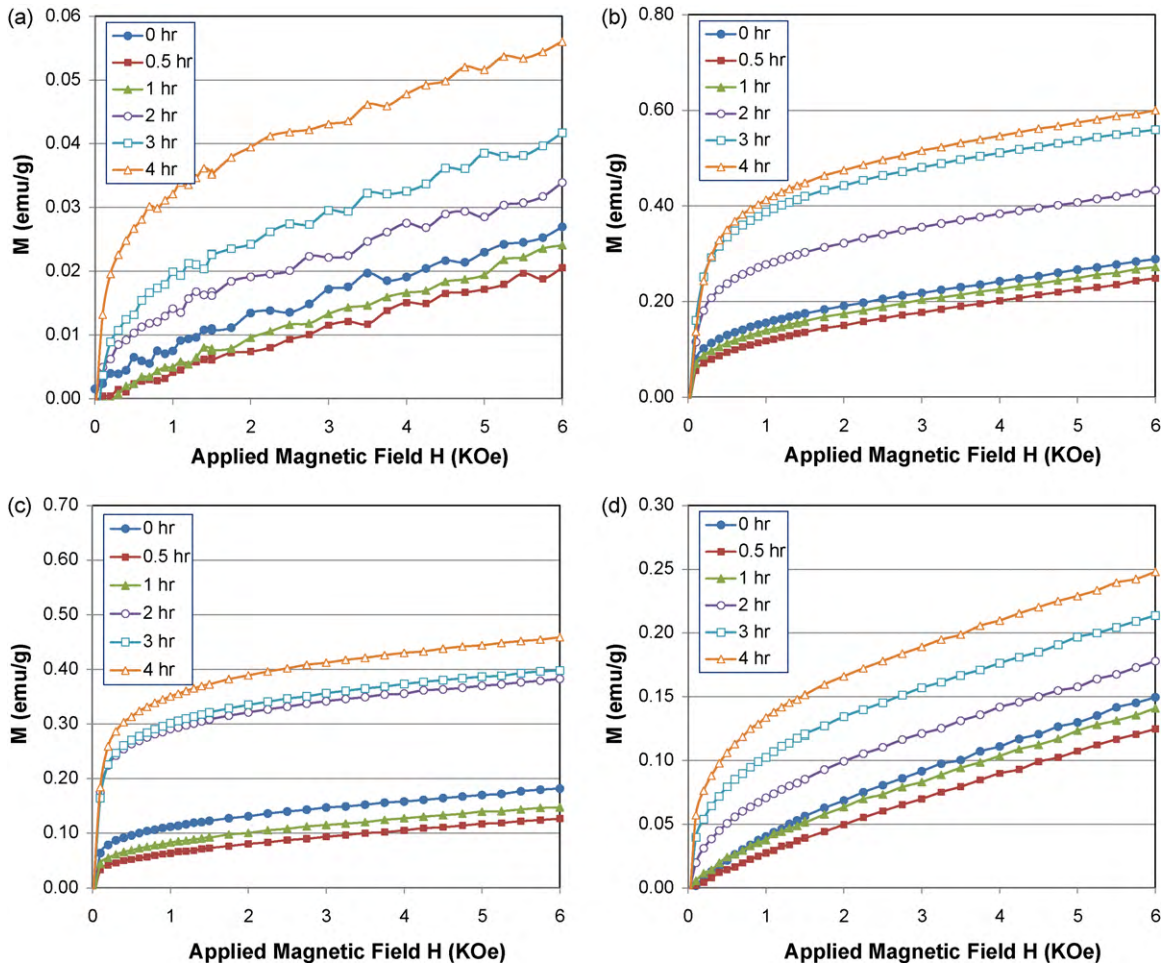

Fig. 6. The magnetic susceptibility curves measured at room temperature for alloys A (a), B (b), C (c), and D (d).

with different etching periods. These curves are plotted in Fig. 6a–d for alloys A–D, respectively. These magnetization curves can be fit to the Langevin function [28]

$$M(H) - \chi_B H = M_S \left\{ \coth\left(\frac{\mu H}{kT}\right) - \frac{kT}{\mu H} \right\} \quad (2)$$

where χ_B is the intrinsic paramagnetic susceptibility of the alloy (estimated by the value of the high field magnetization), M_S is the saturation magnetization of the ferromagnetic metallic Ni or Ni-alloy nanoparticles, μ is the average magnetic moment of each metallic cluster, k is the Boltzmann constant, and T is the absolute temperature. The mass fraction of metallic inclusion can be estimated from the ratio of the measured M_S and the known magnetic susceptibility of pure nickel metal (58.6 emu/g) under the assumption that all clusters are pure Ni and that the ferromagnetic signal is produced solely by Ni nanoparticles. The size of the metallic clusters was computed using μ together with the known moment per Ni atom (0.6 μ_B/Ni [97]). Since different amount of moment per Ni atom was used before [27,28,31], we will use the value normalized to cluster size of Alloy A after a 4 h etch in the following comparison.

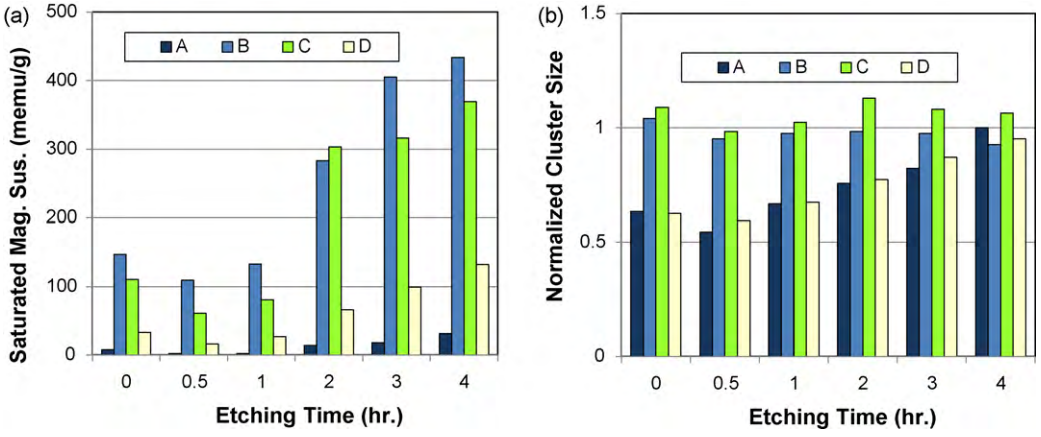

Fig. 7. Evolution of the saturated magnetic susceptibility (a), and normalized cluster size (b) as functions of etching time for alloys A–D.

Both the M_S values and the normalized size of the clusters are listed for each alloy in Table 2 and plotted in Fig. 7a and b. The M_S and the average size of the metallic clusters both decrease in the first half-hour of the etching experiment for all four alloys. This suggests the dissolution of the native oxide formed during powder processing [98]. After this time, a new oxide layer having a higher porosity due to selective leaching is formed. The thickness of this oxide layer increases with the etching time until the accumulated hydrogen slows down further oxidation of the bulk metal. After 4 h of etching, the magnitude of the saturation magnetization is largest for Alloy B, followed by the alloy sequence of C, D, and then A. This order is similar, but not identical to that of the room temperature HRD presented in Section 3.3.1. As we discussed previously (Section 3.1), the M_S values are more strongly correlated with low temperature specific power than with room temperature specific power, as other factors also influence the room temperature high power performance.

The relatively low M_S value observed in the AB_2 alloy can be correlated to the reduced high-rate drain performance found in this sample. The AB_5 alloy shows the largest surface catalytic activity. These studies suggest future developments to optimize the properties of AB_2 and A_2B_7 alloys will benefit from focusing on improving the design of the surface oxide and the metallic clusters in physical size, proximity, structure, and chemical composition through atomic engineering [21] and/or other surface modification methods, such as surface fluorination [62,63], hot charging [99,100], reducing agent [101], wet ball milling [102], and milling with other metals [103] or alloys [104,105].

The evolution of the total volume, surface area, average diameter, and number of metallic Ni clusters, normalized to the values before etching, are shown in Fig. 8a–d. The surface area and number of clusters are estimated using the ratio of the volume and average diameter and the cube of the average diameter, respectively. The surface area of these clusters, which is associated with the total catalytic activity, increases in all four alloys as the etching proceeds. By comparing these individual curves, we are able to make a number of statements concerning the interplay of etching and cluster modification. Alloys A and D show similar features: the number of clusters remains constant after 2 h of etching with the further increase in M_S with etching time arising from the growth of the metallic cluster. The behavior of alloys B and C also exhibit similar characteristics: the size of the clusters remains approximately unchanged throughout the entire etching process, with the increase in M_S arising from an increase in the number of clusters. In the case of Alloy A (AB_2), Zr and V oxidize, become complex ions, and then leach out from the surface. The thickness of the surface remains fixed at about 2000 Å throughout the entire etching process, pointing to a balance between bulk oxidation and oxide dissolution [106]. The longer this sample (Alloy A) sits in the hot alkaline bath, the more metallic nickel is available and thus the diameter of the cluster continues to grow but the number of cluster remains constant. In the case of Alloy B (AB_5) alloy, the rare earth constituents oxidize into a non-soluble passive hydroxide on the surface, which increases in thickness as the etching proceeds [51]. Therefore, new clusters can form in the newly developed oxide region. As the etching proceeds, the amount of surface clusters increases, but the average diameter of these clusters remains unchanged.

3.4.3. TEM studies

TEM analysis was performed on all four alloys after a 4 h etch in 30% KOH solution held at 100 °C. In Fig. 9, panels a and b show images from Alloy A, panels c and d from Alloy B, e from Alloy C,

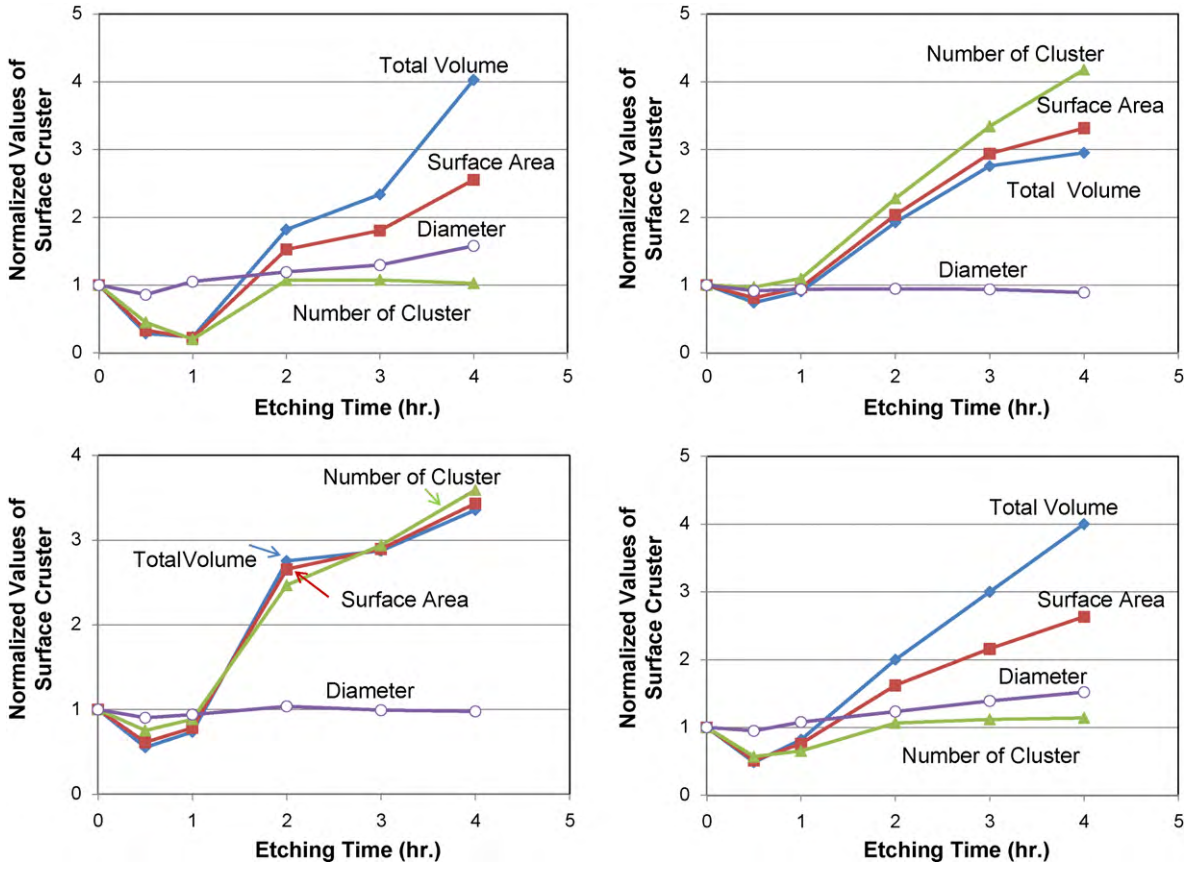

Fig. 8. Total volume, surface area, average diameter, and number of clusters normalized to values from the virgin sample as functions of etching time for alloys A (a), B (b), C (c), and D (d).

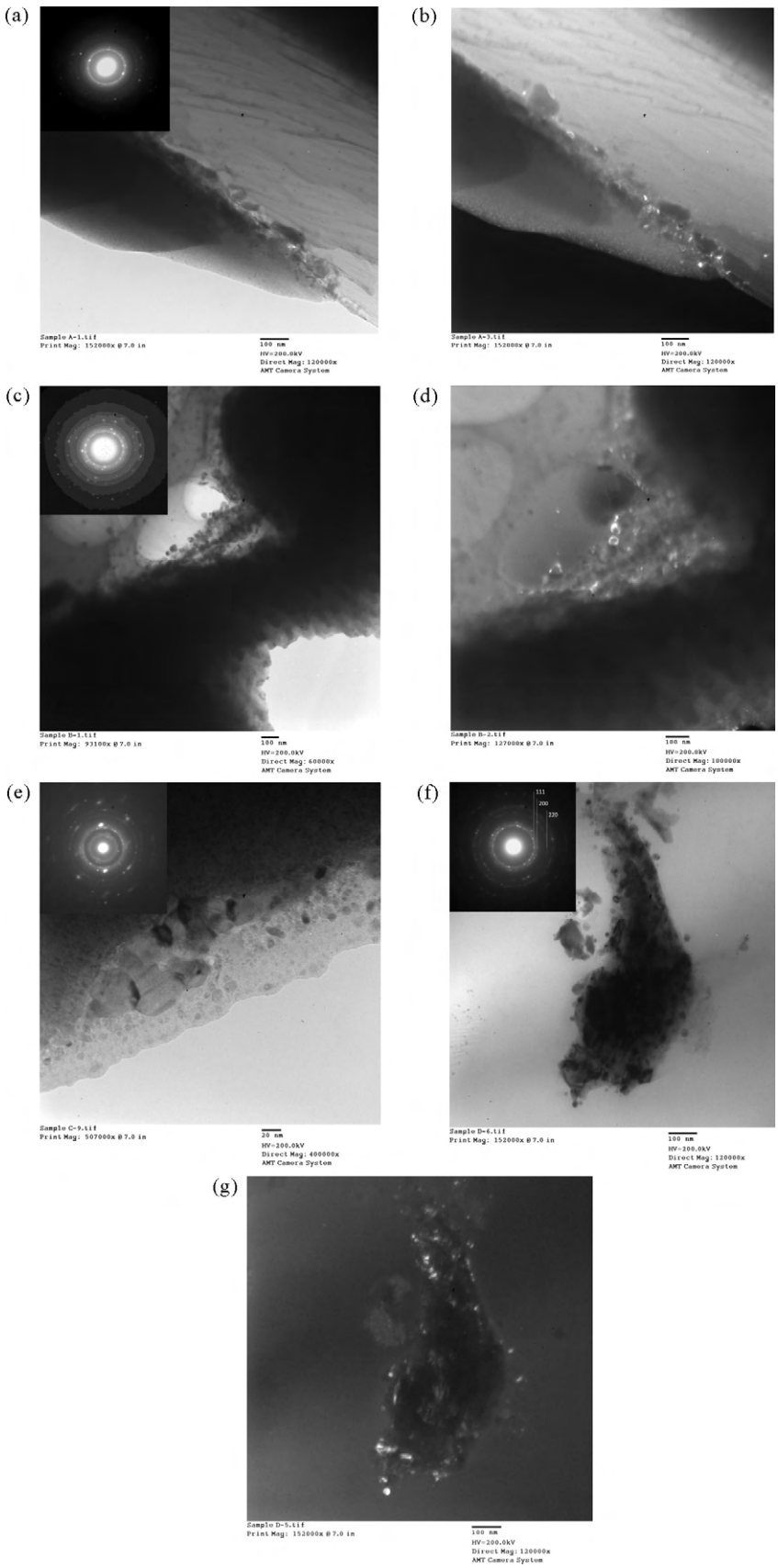

Fig. 9. TEM bright-field micrograph (a), dark-field micrograph (b) from Alloy A, bright-field micrograph (c), dark-field micrograph (d) from Alloy B, bright-field micrograph (e) from Alloy C, bright-field micrograph (f), and dark-field micrograph (g) from Alloy D, etched in 30% KOH at 100 °C for 4 h. The insert in each bright-field micrograph is from the metallic nickel inclusions area with a FCC crystal structure indexed in (f).

and f and g from Alloy D. The bright-field micrographs, Fig. 9a, c, e, and f, show the cross-section of grains from each alloy, showing some small particulates on the surface (note the different magnifications in these images). The selected area electron diffraction patterns measured at the inclusion area are consistent with a Face-Centered-Cubic (FCC) crystal structure (inserts in Fig. 9a, c, e and f). In order to estimate the lattice parameter of the FCC crystal, the camera length was firstly calibrated using the standard sample with evaporated Al nanoparticles. The diameters of the diffraction rings were then measured from which we extracted the lattice parameter of the nanoparticles embedded on the surface of the alloys. The values obtained coincide well with the lattice parameter of metallic nickel. From the dark-field micrographs from the same areas (Fig. 9b, d, and g), the sizes of the largest bright metallic nickel crystallite are estimated to be around 100 Å with nickel particles in the 10–70 Å size range present. From the magnetization measurements, we determined that the differences in electrochemical properties of the various alloys could be mainly attributed to differences in the concentration of metallic nanoclusters embedded in the surface alloy. However, due to the fragility of the surface oxide, it is difficult to extract a reliable estimate of the cluster density using these TEM images, precluding a direct comparison with the magnetization data. We also used EDS to characterize the composition of these metallic nanoparticles. The EDS results in these metallic clusters region measured are $Ni_{62.6}Mn_{27.5}Zr_{3.9}Co_{2.0}Ti_{1.6}V_{1.5}Cr_{0.9}$ (Alloy A), $Ni_{70.3}Co_{21.0}Mn_{3.2}La_{2.2}Ce_{1.4}Nd_{0.9}Al_{0.8}Pr_{0.2}$ (Alloy B), $Ni_{82.6}Co_{14.8}La_{2.1}Mg_{0.5}$ (Alloy C) and Ni (Alloy D). Some matrix elements come from the cross-contamination during sample preparation. Nevertheless, Co and Mn are clearly present in the metallic clusters, as has been reported previously [36,50]. The very fine structure of these metallic inclusions together with location of Co and Mn require further studies by high-resolution TEM.

4. Summary

These electrochemical, structural, and magnetic investigations allow us to draw a number of important conclusions concerning the interplay between metallic nanoparticles embedded in the surface oxide layer and the battery performance of the electrodes. By thorough investigations of four specific alloys, AB_2, AB_5, La–A_2B_7, and Nd–A_2B_7, we have explored the effects of compositional and structural difference in promoting the precipitation of metallic, mainly Ni, nanoclusters and modifying the battery properties. These exhaustive studies, separated into gas phase, half-cell, and etching investigations, are summarized by ranking the properties of the four alloys from largest to smallest, as follows:

Gas phase
Storage capacity $AB_2 > La–A_2B_7 > Nd–A_2B_7 \sim AB_5$
Plateau slope $AB_2 > AB_5 > La–A_2B_7 > Nd–A_2B_7$
Plateau pressure $Nd–A_2B_7 > AB_5 > AB_2 > La–A_2B_7$
PCT hysteresis $La–A_2B_7 > AB_5 > AB_2 > Nd–A_2B_7$
Slope in α phase $Nd–A_2B_7 > AB_5 > La–A_2B_7 > AB_2$
Half-cell
Total capacity $AB_2 > La–A_2B_7 > AB_5 \sim Nd–A_2B_7$
Activation $La–A_2B_7 \sim Nd–A_2B_7 > AB_5 > AB_2$
High-rate dischargeability $AB_5 > Nd–A_2B_7 > La–A_2B_7 > AB_2$
Surface exchange current $AB_5 > La–A_2B_7 > AB_2 > Nd–A_2B_7$
Bulk diffusion $La–A_2B_7 > AB_5 > Nd–A_2B_7 > AB_2$
Etching experiment
Total solution concentration $AB_5 \sim AB_2 \sim Nd–A_2B_7 > La–A_2B_7$
Surface cluster size $La–A_2B_7 > AB_2 \sim Nd–A_2B_7 \sim AB_5$
Total surface cluster volume $AB_5 > La–A_2B_7 > Nd–A_2B_7 > AB_2$
Total cluster surface area $AB_5 > La–A_2B_7 > Nd–A_2B_7 > AB_2$
Number of clusters $AB_5 > La–A_2B_7 > Nd–A_2B_7 > AB_2$

These studies demonstrate that controlling and characterizing the development of metallic Ni nanoclusters, which can be done indirectly using magnetization measurements, is a crucial component of optimizing the properties of electrode materials. Moreover, we find that the AB_5 alloy has the best high-rate dischargeability (associated with metallic nanoclusters) but low total capacity, while the AB_2 alloy has the lowest high-rate dischargeability, but the highest total capacity. These results provide a framework for selecting specific compositions having the best properties for specific applications.

References

[1] S. Nathira Begum, V.S. Muralidharan, C. Ahmed Basha, J. Alloys Compd. 467 (2009) 124.
[2] S.L. Li, W. Chen, D.M. Chen, K. Yang, J. Alloys Compd. 474 (2009) 164.
[3] M. Raju, M.V. Ananth, L. Vijayaraghavan, J. Alloys Compd. 475 (2009) 664.
[4] E.A. Kumar, M.P. Maiya, S.S. Murthy, B. Viswanathan, J. Alloys Compd. 476 (2009) 92.
[5] X. Ma, X. Wei, H. Dong, Y. Liu, J. Alloys Compd. 490 (2010) 548.
[6] Z. Zhou, Y. Song, S. Cui, C. Huang, W. Qian, C. Lin, Y. Zhang, Y. Lin, J. Alloys Compd. 501 (2010) 47.
[7] S. Srivastava, R.K. Upadhyay, J. Power Sources 195 (2010) 2996.
[8] I. Saldan, J. Frenzel, O. Shekhah, R. Chelmowski, A. Birkner, Ch. Wöll, J. Alloys Compd. 470 (2009) 568.
[9] S. Qiu, H. Chu, Y. Zhang, D. Sun, X. Song, L. Sun, F. Xu, J. Alloys Compd. 471 (2009) 453.
[10] M. Shibuya, J. Nakamura, H. Enoki, E. Akiba, J. Alloys Compd. 475 (2009) 543.
[11] M. Gao, H. Miao, Y. Zhao, Y. Liu, H. Pan, J. Alloys Compd. 484 (2009) 249.
[12] K. Young, M.A. Fetcenko, F. Li, T. Ouchi, J. Koch, J. Alloys Compd. 468 (2009) 482.
[13] K. Young, M.A. Fetcenko, T. Ouchi, F. Li, J. Koch, J. Alloys Compd. 469 (2009) 406.
[14] K. Young, T. Ouchi, J. Koch, M.A. Fetcenko, J. Alloys Compd. 477 (2009) 749.
[15] K. Young, T. Ouchi, W. Mays, B. Reichman, M.A. Fetcenko, J. Alloys Compd. 480 (2009) 434.
[16] K. Young, M.A. Fetcenko, J. Koch, K. Morii, T. Shimizu, J. Alloys Compd. 486 (2009) 559.
[17] K. Young, T. Ouchi, B. Reichman, W. Mays, R. Regmi, G. Lawes, M.A. Fetcenko, A. Wu, J. Alloys Compd. 489 (2010) 202.
[18] M. Gao, S. Zhang, H. Miao, Y. Liu, H. Pan, J. Alloys Compd. 489 (2010) 552.
[19] K. Young, R. Regmi, G. Lawes, T. Ouchi, B. Reichman, M.A. Fetcenko, A. Wu, J. Alloys Compd. 490 (2010) 282.
[20] Y. Zhao, M. Gao, Y. Liu, L. Huang, H. Pan, J. Alloys Compd. 496 (2010) 454.
[21] S.R. Ovshinsky, M.A. Fetcenko, J. Ross, Science 260 (1993) 176.
[22] M.A. Fetcenko, S.R. Ovshinsky, B.S. Chao, B. Reichman, US Patent 5,536,591 (1996).
[23] M.A. Fetcenko, S.R. Ovshinsky, K. Young, B. Reichman, C. Fierro, J. Koch, W. Mays, T. Ouchi, B. Sommers, A. Zallen, J. Alloys Compd. 330–332 (2002) 752.
[24] M.A. Fetcenko, S.R. Ovshinsky, K. Young, B. Reichman, T. Ouchi, J. Koch, W. Mays, US Patent 6,830,725 (2004).
[25] P. Termsuksawad, S. Niyomsoan, R.B. Goldfarb, V.I. Kaydanov, D.L. Olson, B. Mishra, Z. Gavra, J. Alloys Compd. 373 (2004) 86.
[26] M.A. Fetcenko, S.R. Ovshinsky, B. Reichman, K. Young, C. Fierro, J. Koch, A. Zallen, W. Mays, T. Ouchi, J. Power Sources 165 (2007) 544.
[27] L. Schlapbach, A. Seiler, F. Stucki, H.C. Siegmann, J. Less-Commun. Met. 73 (1980) 145.
[28] F. Stucki, L. Schlapbach, J. Less-Commun. Met. 74 (1980) 143.
[29] L. Schlapbach, F. Stucki, A. Seiler, H.C. Siegmann, J. Magn. Magn. Mater. 15–18 (1980) 1271.
[30] L. Schlapbach, F. Stucki, A. Seiler, H.C. Siegmann, Surf. Sci. 106 (1981) 157.
[31] F. Stucki, J. Appl. Phys. 53 (1982) 2643.
[32] G.H. Kim, C.H. Chun, S.G. Lee, J.Y. Lee, Scripta Metall. Mater. 29 (1993) 485.
[33] F. Meli, T. Sakai, A. Züttle, L. Schlapbach, J. Alloys Compd. 221 (1995) 284.
[34] D.P. Broom, M. Kemali, D.K. Ross, J. Alloys Compd. 293–295 (1999) 255.
[35] K. Suzuki, K. Ishikawa, K. Aoki, Mater. Trans. JIM 41 (2000) 581.
[36] F. Maurel, B. Knosp, M. Backhaus-Ricoult, J. Electrochem. Soc. 147 (2000) 78.
[37] M. Ayari, V. Paul-Boncour, J. Lamloumi, A. Percheron-Guegan, J. Magn. Magn. Mater. 242–245 (2002) 850.
[38] W.K. Li, K. Ikeda, Y. Nakamori, S. Orimo, K. Yakushiji, K. Takanashi, H. Ohyama, K. Nakatsuji, Y. Dansui, Acta Mater. 55 (2007) 481.
[39] R. Kikuyama, Japan Patent Publication 2000-90920 (2000).
[40] L.T. Tai, B.T. Hang, N.P. Thuy, T.D. Hieh, J. Magn. Magn. Mater. 262 (2003) 485.
[41] T. Ueda, Japan Patent Publication 2001-135311 (2001).
[42] K. Komori, H. Matsuda, Japan Patent Publication 2000-357508 (2000).
[43] K. Kinoshita, K. Muta, S. Towata, Japan Patent Hei11-222601 (2001).
[44] T. Ueda, Japan Patent Publication 2002-25546 (2002).
[45] Y. Okada, Japan Patent Publication 2002-256301 (2002).
[46] S. Ito, N. Morishita, Japan Patent Publication 2004-11004 (2004).
[47] H. Oyama, K. Nakatsuji, Japan Patent Publication 2007-115672 (2007).
[48] V.D. Dobrovolsky, S.N. Yendrzheevskaya, A.K. Sinelnichenko, V.V. Skorokhod, O.Y. Khyzhun, Int. J. Hydrogen Energy 21 (1996) 1061.

[49] V.D. Dobrovolsky, Y.M. Solonin, V.V. Skorokhod, O.Y. Khyzhun, J. Alloys Compd. 253–254 (1997) 488.
[50] M. Backhaus-Ricoult, J.L. Vignes, G. Lorang, B. Knosp, J. Alloys Compd. 253–254 (1997) 492.
[51] L. Schlapbach, A. Seiler, H.C. Siegmann, T.V. Waldkirch, P. Zurcher, Int. J. Hydrogen Energy 4 (1979) 21.
[52] F. Meli, L. Schlapbach, J. Less-Commun. Met. 172–174 (1991) 1252.
[53] D. Song, X. Gao, Y. Zhang, D. Lin, Z. Zhou, G. Wang, P. Shen, J. Alloys Compd. 199 (1993) 161.
[54] H. Wang, L. Han, H. Hu, D.O. Northwood, J. Alloys Compd. 470 (2009) 539.
[55] Y.M. Solonin, V.D. Dobrovolsky, O.Y. Khyzhun, in: M.D. Hampton, D.V. Schur, S.Y. Zaginaichenko, V.I. Trefilov (Eds.), Hydrogen Materials Science and Chemistry of Metal Hydrides, Kluwer Academic Publishers, Netherlands, 2002, p. 415.
[56] S. Morishita, Y. Kondo, Y. Oya, S. Towata, K. Abe, J. Chem. Soc. Jpn. 6 (1999) 369.
[57] K. Young, M.A. Fetcenko, US Patent 6,120,936 (2000).
[58] K. Young, M.A. Fetcenko, S.R. Ovshinsky, US Patent 6,461,766 (2002).
[59] D.Y. Yan, Q. Cheng, T. Cui, J. Alloys Compd. 293–295 (1999) 809.
[60] H.J. Lee, D.C. Yang, C.J. Park, C.N. Park, H.J. Jang, Int. J. Hydrogen Energy 34 (2009) 481.
[61] X.L. Wang, S. Suda, J. Alloys Compd. 231 (1995) 380.
[62] D.Y. Yan, Y.M. Sun, S. Suda, J. Alloys Compd. 231 (1995) 387.
[63] Z.P. Li, E. Higuchi, B.H. Liu, S. Suda, J. Alloys Compd. 293–295 (1999) 593.
[64] B.H. Liu, Z.P. Li, E. Higuchi, S. Suda, J. Alloys Compd. 293–295 (1999) 702.
[65] Z.P. Li, E. Higuchi, B.H. Liu, S. Suda, Electrochim. Acta 45 (2000) 1773.
[66] X. Gao, D. Song, Y. Zhang, Z. Zhou, W. Zhang, M. Wang, P. Shen, J. Alloys Compd. 229 (1995) 268.
[67] Y. Kuribayashi, H. Sugahara, M. Ishii, S. Shima, US Patent 6,235,130 (2001).
[68] P. Zhang, X. Wang, J. Tu, G. Chen, J. Rare Earths 27 (2009) 510.
[69] S. Yamakawa, K. Saito, S. Towata, S. Morishita, S. Hibino, K. Kuroda, H. Saka, J. Jpn. Inst. Metals 67 (2003) 53.
[70] A.N. Lassegne-Jackson, B. Mishra, D.L. Olsen, Mater. Manuf. Processes 22 (2007) 433.
[71] K. Young, T. Ouchi, M.A. Fetcenko, J. Alloys Compd. 476 (2009) 774.
[72] K. Young, T. Ouchi, M.A. Fetcenko, US Patent 7,344,677 (2008).
[73] F.A. Fetcenko, K. Young, S.R. Ovshinsky, T. Ouchi, US Patent 7,393,500 (2008).
[74] Y. Osumi, Suiso-kyuzo-goukin no Syurui to Sono, new ed., Agune Technology Center, Tokyo, Japan, 1999, p. 497.
[75] T. Kohno, H. Yoshida, F. Kawashima, T. Inaba, I. Sakai, M. Yamamoto, M. Kanda, J. Alloys Compd. 311 (2000) L5.
[76] H. Teraoka, Presented in Batteries 2007, September 26–28, Nice, France. Article available from http://www.eneloop.info/fileadmin/EDITORS/ENELOOP/ARTICLES/Teraoka_Article_EN.pdf.
[77] K. Young, T. Ouchi, M.A. Fetcenko, J. Alloys Compd. 480 (2009) 428.
[78] J. Cao, X. Gao, D. Lin, X. Zhou, H. Yuan, D. Song, P. Shen, J. Power Sources 93 (2001) 141.
[79] M. Wu, H. Wu, Y. Wang, C. Wan, J. Alloys Compd. 302 (2000) 248.
[80] M.P. Sridhar, W. Zhang, K. Petrov, S. Srinivasan, G.D. Adzic, J.R. Johnson, J.J. Reilly, R.B. Schwarz, Hydrogen and metal hydride batteries, in: P.D. Bennett, T. Sakai (Eds.), Electrochem. Soc. Proc., 94–27, 1994, p. 111.
[81] J. Kleperis, G. Wójcik, A. Czerwinski, J. Skowronski, M. Kopczyk, M. Beltowska-Brzezinska, J. Solid State Electrochem. 5 (2001) 229.
[82] M.V. Ananth, M. Raju, K. Manimaran, G. Balachandran, L.M. Nair, J. Power Sources 167 (2007) 228.
[83] M.V. Ananth, M. Ganesan, N.G. Renganathan, S. Lakshmi, Int. J. Hydrogen Energy 34 (2009) 356.
[84] Y. Liu, H. Oan, M. Gao, R. Li, Y. Lei, J. Alloys Compd. 389 (2005) 281.
[85] H. Pan, R. Li, M. Gao, Y. Liu, Y. Lei, Q. Wang, Int. J. Hydrogen Energy 31 (2006) 1188.
[86] H. Pan, Y. Liu, M. Gao, Y. Lei, Q. Wang, J. Electrochem. Soc. 152 (2005) A326.
[87] Y. Fukai, The Metal-Hydrogen System, in: Springer Series in Materials Science 21, Springer-Verlag, Berlin Heidelberg, 1993, p. 207.
[88] H. Wipf, Hydrogen in metals III, properties and applications, in: H. Wipf (Ed.), Topics in Applied Physics, 73, Springer-Verlag, Berlin Heidelberg, 1997, p. 52.
[89] Y. Hukai, K. Tanaka, H. Uchida, Hydrogen and Metal, Uchida Rokakuho Publishing Co., Tokyo, 1998, p. 119.
[90] V.M. Sidorenko, I.I. Sidorak, Fiziko-Khim. Mekhanika Materialov 9 (1973) 12.
[91] K.C. Hong, K. Sapru, in: T.N. Veziroğlu, Y. Zhu, D. Bao (Eds.), Hydrogen Systems, 1, Pergamon Press, Oxdord, 1994, p. 487.
[92] T. Nishina, H. Ura, I. Uchida, J. Electrochem. Soc. 144 (1997) 1273.
[93] B. Reichman, S. Venkatesan, M.A. Fetcenko, K. Jeffries, S. Stahl, C. Bennett, US Patent 4,716,088 (1987).
[94] S. Rodrigues, N. Munichandraiah, A.K. Shukla, Bull. Mater. Sci. 23 (2000) 383.
[95] J.J. Reilly, G.D. Adzic, J.R. Johnson, T. Vogt, S. Mukerjee, J. McBreen, J. Alloys Compd. 293–295 (1999) 569.
[96] H. Senoh, M. Ueda, H. Inoue, N. Furukawa, C. Iwakura, J. Alloys Compd. 266 (1998) 111.
[97] R. Mallik, P.L. Paulose, E.V. Sampthkaumaran, S. Patil, V. Nagarajan, Phys. Rev. B55 (1997) 8369.
[98] B. Reichman, W.C. Mays, K. Young, M.A. Fetcenko, S.R. Ovshinsky, T. Ouchi, Electrochem. Soc. Proc. 98–15 (1998) 111.
[99] J.H. Jung, H.H. Lee, D.M. Kim, B.H. Liu, K.Y. Lee, J.Y. Lee, J. Alloys Compd. 253 (1997) 652.
[100] B. Yu, L. Chen, M. Wen, M. Tong, D. Chen, J. Mater. Sci. Technol. 17 (2001) 247.
[101] C. Iwakura, I. Kim, N. Matsui, H. Inoue, M. Matsuoka, Electrochim. Acta 40 (1995) 561.
[102] B. Liu, Z. Li, A. Okutsu, S. Suda, J. Alloys Compd. 296 (2000) 148.
[103] C. Jung, J. Kim, K. Lee, J. Alloys Compd. 267 (1998) 265.
[104] Z. Chen, Z. Chen, K. Huang, P. Huang, J. Alloys Compd. 293–295 (1999) 712.
[105] S. Han, Z. Zhang, M. Zhao, Y. Zheng, Int. J. Hydrogen Energy 31 (2006) 563.
[106] H. Chu, Y. Zhang, L. Sun, S. Qui, F. Xu, H. Yuan, Q. Wang, C. Dong, Int. J. Hydrogen Energy 32 (2007) 3363.